The Astrophysical Journal, 984:181 (16pp), 2025 May 9 https://doi.org/10.3847/1538-4357/adc73b

The Climates and Thermal Emission Spectra of Prime Nearby Temperate Rocky Exoplanet Targets

Tobi Hammond[1,2,3,4], Thaddeus D. Komacek[4,5,6], Ravi K. Kopparapu[2,14], Thomas J. Fauchez[2,7], Avi M. Mandell[2], Eric T. Wolf[6,8], Vincent Kofman[2,7], Stephen R. Kane[9], Ted M. Johnson[2,10,11], Anmol Desai[2,3,12], Giada Arney[2], and Jaime S. Crouse[2,13]

[1] Department of Earth, Atmospheric, and Planetary Science, Purdue University, West Lafayette, IN 47907, USA
[2] NASA Goddard Space Flight Center, Greenbelt, MD 20771, USA
[3] Center for Research and Exploration in Space Science and Technology, NASA Goddard Space Flight Center, Greenbelt, MD 20771, USA
[4] Department of Astronomy, University of Maryland, College Park, MD 20742, USA; tad.komacek@physics.ox.ac.uk
[5] Department of Physics (Atmospheric, Oceanic and Planetary Physics), University of Oxford, Oxford, OX1 3PU, UK
[6] Blue Marble Space Institute of Science, Seattle, WA 98104, USA
[7] American University, 4400 Massachusetts Avenue, NW, Washington, DC 20016, USA
[8] Laboratory for Atmospheric and Space Physics, University of Colorado Boulder, Boulder, CO 80303, USA
[9] Department of Earth and Planetary Sciences, University of California, Riverside, CA 92521, USA
[10] Nevada Center for Astrophysics, University of Nevada, Las Vegas, 4505 South Maryland Parkway, Las Vegas, NV 89154, USA
[11] Department of Physics and Astronomy, University of Nevada, Las Vegas, 4505 South Maryland Parkway, Las Vegas, NV 89154, USA
[12] Southeastern Universities Research Association, Washington, DC 20005, USA
[13] Johns Hopkins University, Baltimore, MD 21218, USA
Received 2024 November 21; revised 2025 March 17; accepted 2025 March 28; published 2025 May 8

Abstract

Over the course of the past decade, advances in radial velocity and transit techniques have enabled the detection of rocky exoplanets in the habitable zones of nearby stars. Future observations with novel methods are required to characterize this sample of planets, especially those that are nontransiting. One proposed method is the Planetary Infrared Excess (PIE) technique, which would enable the characterization of nontransiting planets by measuring the excess IR flux from the planet relative to the star's spectral energy distribution. In this work, we predict the efficacy of future observations using the PIE technique by potential future observatories such as the MIRECLE mission concept. To do so, we conduct a broad suite of 21 general circulation model (GCM) simulations, with ExoCAM, of seven nearby habitable zone targets for three choices of atmospheric composition with varying partial pressure of CO_2. We then construct thermal phase curves and emission spectra by post-processing our ExoCAM GCM simulations with the Planetary Spectrum Generator (PSG). We find that all cases have distinguishable carbon dioxide and water features assuming a 90° orbital inclination. Notably, we predict that CO_2 is potentially detectable at 15 μm with MIRECLE for at least four nearby known nontransiting rocky planet candidate targets in the habitable zone: Proxima Centauri b, GJ 1061 d, GJ 1002 b, and Teegarden's Star c. Our ExoCAM GCMs and PSG post-processing demonstrate the potential to observationally characterize nearby nontransiting rocky planets and better constrain the potential for habitability in our solar neighborhood.

Unified Astronomy Thesaurus concepts: Exoplanet atmospheric dynamics (2307); Exoplanet atmospheres (487); Planetary climates (2184); Astrobiology (74); Planetary atmospheres (1244)

1. Introduction

There has been a rapid advance in the discovery space of potentially habitable exoplanets over the past decade, including the discoveries of Proxima Centauri b (G. Anglada-Escudé et al. 2016), TRAPPIST-1e, f, g (M. Gillon et al. 2017), TOI-700d, e (J. E. Rodriguez et al. 2020; E. A. Gilbert et al. 2023), Wolf 1069 b (D. Kossakowski et al. 2023), and LP 890-9 c (L. Delrez et al. 2022), among others. These detections are opening up a new era of exoplanet science that began with the commissioning of JWST, enabling IR spectral characterization to constrain the presence or absence of atmospheres on rocky exoplanets (T. P. Greene et al. 2023; J. Lustig-Yaeger et al. 2023; E. M. May et al. 2023; S. Zieba et al. 2023; M. Weiner Mansfield et al. 2024; Q. Xue et al. 2024). JWST is expected to be able to probe the atmospheric composition of nearby transiting (J. Lustig-Yaeger et al. 2019; T. Mikal-Evans 2022) and possibly nontransiting exoplanets (L. Kreidberg & A. Loeb 2016; K. B. Stevenson & Space Telescopes Advanced Research Group on the Atmospheres of Transiting Exoplanets 2020) orbiting M dwarf stars, though stellar activity can be a significant challenge (O. Lim et al. 2023; B. V. Rackham & J. de Wit 2024). Additionally, future mission concepts targeting UV/optical/near-IR imaging, such as the Habitable Worlds Observatory, as well as mid-IR (MIR) spectroscopy and phase curves, with missions such as MIRECLE (A. M. Mandell et al. 2022) and the Far-IR Surveyor and LIFE (S. P. Quanz et al. 2022) flagships, would further advance our understanding of rocky exoplanets by enabling characterization of their atmospheres.

Many of the nearby rocky planets in the habitable zone are nontransiting and have close-in orbits around M dwarf host stars, because our current detection methods favor finding Earth-sized planets around smaller and less massive stars

[14] CHAMPs Collaboration.

(C. Lovis & D. Fischer 2010; J. Winn 2010). Characterizing these planets requires the development of alternate methods beyond primary and secondary eclipse spectroscopy or traditional direct imaging to observationally characterize their atmospheres. A clear path forward for ground-based observatories is the combination of high-dispersion spectroscopy with high-contrast imaging (I. Snellen et al. 2015; S. R. Vaughan et al. 2024) that can theoretically reach contrast limits of 10^{-10}.

One recently developed method for space-based observatories is the Planetary Infrared Excess (PIE) technique (K. B. Stevenson & Space Telescopes Advanced Research Group on the Atmospheres of Transiting Exoplanets 2020). The PIE technique targets the planetary infrared excess (as the name suggests) and its presence in the unresolved combined stellar and planetary spectra. PIE attempts to isolate the fraction of light originating from the planet by accurately modeling the stellar spectral energy distribution. PIE is similar to the detection of debris disks via IR excess, in that it separates the spectra of the planet and star in order to isolate the planetary thermal emission. The PIE technique has been demonstrated to be feasible for simulated JWST observations of hot Jupiters (J. Lustig-Yaeger et al. 2021) as well as simulated observations of Proxima Centauri (A. M. Mandell et al. 2022) and the TRAPPIST-1 system (L. C. Mayorga et al. 2023). Using a similar technique but with higher spectral resolution, I. A. G. Snellen et al. (2017) proposed that high-pass spectral filtering of planetary thermal emission could enable the detection of the 15 μm CO_2 band with MIRI MRS.

The PIE technique has the best potential to constrain the planetary climate when measuring the direct planetary thermal emission over many orbital phases. As a result, PIE is strongly dependent on the spatial pattern of thermal flux from the planet as it orbits its host star. However, to date, there have been no multidimensional model predictions for the PIE technique. The PIE technique is further best suited to characterizing nearby planets orbiting small cool stars, given the requirement that the planetary flux at long wavelengths must be above the noise floor (K. B. Stevenson & Space Telescopes Advanced Research Group on the Atmospheres of Transiting Exoplanets 2020). Studies with three-dimensional (3D) general circulation models (GCMs) of temperate rocky planets in the habitable zones of small K and M dwarf systems have found that their temperature and cloud patterns are strongly inhomogeneous, leading to a strong phase dependence in the resulting thermal emission (J. Yang et al. 2013; D. Koll & D. Abbot 2016; M. Turbet et al. 2016; E. Wolf 2017; M. Way et al. 2018; A. Shields 2019; K. Batra & S. L. Olson 2024; A. H. Lobo & A. L. Shields 2024). A range of previous GCM simulations have been applied to study the potential climate dynamics of nearby temperate rocky planets, including Proxima Centauri b (M. Turbet et al. 2016; I. Boutle et al. 2017; N. Lewis et al. 2018; A. Del Genio et al. 2019; A. Salazar et al. 2020; P. De Luca et al. 2024), TRAPPIST-1e (E. Wolf 2017; M. Turbet et al. 2018, 2022; T. J. Fauchez et al. 2019, 2022; E. May et al. 2021; D. E. Sergeev et al. 2022; Y. Rotman et al. 2023; M. T. Mak et al. 2024), TRAPPIST-1d (E. Wolf 2017; M. Turbet et al. 2023), and TOI-700d (G. Suissa et al. 2020b). Though there have been a range of generalized studies of temperate rocky planets orbiting M dwarf stars with varying planetary parameters (e.g., M. Joshi et al. 1997; T. Merlis & T. Schneider 2010; J. Yang et al. 2014; D. Koll & D. Abbot 2016; Y. Fujii et al. 2017; A. Shields 2019; E. T. Wolf et al. 2019; G. Suissa et al. 2020a; E. Macdonald et al. 2022; M. Turbet et al. 2023), there has not yet been a broad and uniform study of the climates of the range of specific nearby habitable zone targets that be characterized in thermal emission with PIE.

In this work, we conduct a suite of GCM simulations of seven nearby (1.3–32.4 pc) temperate, potentially rocky planets orbiting late-type stars: LP 890-9 c, TRAPPIST-1e, GJ 1002 b, Proxima Centauri b, Wolf 1069 b, GJ 1061 d, and Teegarden's Star c. In order to study their broad ranges of potential climate states, we vary the primary greenhouse gas CO_2 over a wide range for each planet case, from approximately Earth-like to a thick 2 bar CO_2 atmosphere. We post-process our GCM simulations to predict thermal emission spectra and the detectability of spectral features with the PIE technique.

This manuscript is organized as follows. We first describe both our ExoCAM GCM and NASA Planetary Spectrum Generator (PSG) model setup in Section 2. We then present our simulated climate and observable properties of seven high-priority nearby rocky planet targets in Section 3. We discuss our findings, limitations, and future work in Section 4, and we state the key takeaways in Section 5.

2. Methods

2.1. GCM Model

To simulate the atmospheres of the selected seven synchronously rotating rocky exoplanets orbiting M dwarf stars, we use ExoCAM,[15] a 3D GCM (E. Wolf et al. 2022). ExoCAM has been used to investigate the climates of exoplanets across a broad range of parameter spaces (R. Kopparapu et al. 2017; E. Wolf 2017; J. Haqq-Misra et al. 2018; H. Yang et al. 2019; G. Suissa et al. 2020a; M. Wei et al. 2020; E. Wolf et al. 2020, 2022; Y. Rotman et al. 2023; V. Garcia et al. 2024; T. Hammond & T. D. Komacek 2024; R. Zhan et al. 2024) and various model intercomparison studies (T. J. Fauchez et al. 2022; D. E. Sergeev et al. 2022; M. Turbet et al. 2022). ExoCAM is a publicly available modified version of the Community Earth System Model (CESM), version 1.2.1 (R. Neale et al. 2010). ExoCAM is coupled to ExoRT,[16] a flexible two-stream correlated-k radiative transfer scheme.

We conducted 21 ExoCAM GCMs for seven planet targets (Table 1), with three atmospheric scenarios for each planet, with pCO_2 varying from 100 μbar to 2 bar (Table 2).

We choose this set of planet targets in order to both benchmark against previous studies (for, e.g., TRAPPIST-1e and Proxima Centauri b) as well as to conduct simulations of planets that are expected to be promising targets for the PIE technique. For the nontransiting planets in the sample, for simplicity, we take the mass to be the minimum mass from radial velocity observations and we use the radius calculated assuming an Earth-like bulk composition (see Table 1 for the sources of these radial velocity masses as well as our other assumed planetary parameters).

All of our 21 ExoCAM GCMs make the same set of the following key assumptions. First, we assume that each planet is spin-synchronized, with a rotation period equal to its orbital period. We further assume that each planet has zero obliquity and zero eccentricity, consistent with tidal locking. We note

[15] https://github.com/storyofthewolf/ExoCAM
[16] https://github.com/storyofthewolf/ExoRT

Table 1
Planetary Parameters Adopted for Our GCM Simulations

Planet Name	Radius ($R_\oplus$)	g (ms^{-2})	Period (days)	Instellation ($S_\oplus$)	Stellar Temp (K)	Distance (pc)
LP 890-9c[a]	1.37	13.10	8.46	0.91	2871	32.43
TRAPPIST-1e[b]	0.92	8.01	6.10	0.646	2566	12.47
GJ 1002 b[c]	1.10	8.74	10.35	0.67	3024	4.85
Proxima Centauri b[d]	1.10	10.88	11.20	0.645[e]	3050	1.30
Wolf 1069 b[f]	1.08	10.58	5.60	0.652	3158	9.58
GJ 1061 d[g]	1.23	10.61[h]	13.03	0.60	2953	3.67
Teegarden's Star c[i]	1.05	9.86[h]	11.41	0.37	2904	3.83

Notes. References for these parameters are shown below.
[a] L. Delrez et al. (2022).
[b] E. Agol et al. (2021).
[c] A. Suárez Mascareño et al. (2023).
[d] M. Turbet et al. (2016).
[e] I. A. Boutle et al. (2017).
[f] D. Kossakowski et al. (2023).
[g] S. Dreizler et al. (2020).
[h] Á Boldog et al. (2024).
[i] M. Zechmeister et al. (2019).

Table 2
Parameter Choices for Our Suite of ExoCAM GCM Simulations

CO_2 (bar)	N_2(bar) (bar)	Obliquity (deg)	Eccentricity
0.0001	1	0	0
0.1	1	0	0
2	0	0	0

Note. We conduct three simulations for each planet with varying pCO_2, for a total of 21 GCM simulations.

that because each planet in the sample is cool and is expected to have a ratio of radiative to rotational timescales $\tau_{rad}/P_{rot} > 1$, the effects of seasonality on climate would be minimal regardless (K. Ohno & X. Zhang 2019). We assume that each target is an aquaplanet with a global surface slab ocean with a depth of 50 m and zero ocean heat transport. We allow sea ice to form thermodynamically (C. Bitz et al. 2012), but we do not include sea ice drift (J. Yang et al. 2023).

Our simulations have a horizontal resolution of $4° \times 5°$ and 40 atmospheric levels. They have a 30 minutes physics time step, a ratio of physics to dynamical time step, termed "nsplit" in CESM, of 32 (leading to a dynamical time step of 56.25 s), and a 60 minutes radiative time step. Each simulation is run until equilibrium in both the top-of-atmosphere net radiation and globally averaged surface temperature. In the following, we only show results from the average of the last 10 yr of model output.

2.2. PSG

We use the publicly available NASA PSG[17] (G. L. Villanueva et al. 2018, 2022), specifically its Global Emission Spectra (GlobES) module[18] (V. Kofman et al. 2024), to simulate thermal emission spectra from our ExoCAM outputs. To simulate idealized PIE observations with PSG, we divide the planetary thermal emission by the total flux of the unresolved system, yielding the planet–star contrast. This technique assumes complete knowledge of the stellar spectrum—i.e., that it can be removed from the total spectrum without resulting in biases in the planetary spectrum. We also assume that the star is noiseless in the initial PIE calculation, for simplicity. To relax these assumptions would require more complicated retrieval methods (T. M. Johnson et al. 2025, in preparation).

In order to conduct our PSG GlobES post-processing calculations, we take the ExoCAM output atmospheric composition profiles for H_2O, N_2, and CO_2 at each longitude and latitude, as well as the liquid water cloud and ice cloud profiles. Our PSG GlobES calculations take in the 3D GCM output as input and then compute the thermal emission spectra for a specific orbital phase (or viewing geometry), as in T. M. Johnson et al. (2025). We include Rayleigh scattering, atmospheric refraction, and collision-induced absorption in our calculations, which are all on by default in PSG GlobES. Relevant in particular for this study is the H_2O–H_2O collision-induced absorption, which is parameterized from the MT_CKD continuum (V. Kofman & G. L. Villanueva 2021) and adopted both in PSG and ExoCAM.

We calculate thermal emission spectra in the MIR from 5 to 18 μm for a MIRECLE-like telescope with a diameter of 1.5 m. The telescope parameters as well as the assumed noise parameters are listed in Table 3 and are the default settings for MIRECLE in PSG (A. M. Mandell et al. 2022). To provide accurate reflection of our ExoCAM models in PSG, we set the spatial binning value to 3, in order to minimize the computation time with minimal effect on the simulated observations. We assume an integration time of 30 days for all noise calculations, taking into account the phase variations over multiple orbital

[17] https://psg.gsfc.nasa.gov/, https://github.com/nasapsg

[18] https://psg.gsfc.nasa.gov/apps/globes.php

Table 3
Instrumental Parameter Choices for Our PSG Radiative Transfer Post-processing Calculations

Telescope Parameter	Value	Noise Parameter	Value
Telescope Diameter (m)	1.5	Number of Pixels	8
Field of View (arcsec)	6	Read Noise (e^-)	16.8
Resolving Power (RP)	50	Dark Rate (e^-/s^{-1})	100
Wavelength Coverage (μm)	5–18	Optics temperature (K)	35
Exposure Time (sec)	60	Optics Emissivity	0.1
		Total Throughput	0.7

phases of each target in our PIE calculations with PSG/GlobES.

2.3. Model Limitations

The simulations presented in this work are idealized, in order to explore the possible parameter spaces of nearby rocky planet targets and guide potential observational characterizations. Notably, in our GCMs, we assume only three possible atmospheric compositions for each planet, all of which presume that N_2 or CO_2 is the dominant gas. All simulations further assume tidal locking, with a 1:1 spin–orbit ratio. Additionally, note that the radii we choose for nontransiting planets assume a broadly Earth-like interior composition, even though compression will increase the bulk density of super-Earth-mass planets (D. Valencia et al. 2006).

In addition, our post-processed observations with PSG use time-averaged GCM outputs rather than snapshots to predict the observable spectra and phase curves, but previous work has shown that time variability may impact spectra (E. May et al. 2021; X. Song & J. Yang 2021). As a result, spectra at a specific orbital phase could differ from orbit to orbit—this is neglected here. We also limit our phase range for the post-processing, rather than simulating the spectra over a full orbit.

These idealized setups of our GCMs and radiative transfer post-processing should be kept in mind when viewing the results from these simulations in the following sections. We discuss these and other limitations of the study in greater detail in Section 4.3.

3. Results

3.1. ExoCAM GCMs

3.1.1. Planetary Climate

We first present the simulated climate dynamics from our 21 total cases of seven different nearby rocky planets. Figure 1 shows surface temperature maps (both in filled and open contours) for each of the seven targets (rows) for varying pCO_2 (columns). Note also that we provide a table summarizing the global mean GCM output in the Appendix. The targets are listed in order of decreasing instellation from top to bottom, and all subplots share a color scheme for intercomparison.

As expected, we find that for a given pCO_2, the peak dayside temperature and minimum nightside temperature increase with increasing instellation. We also find that the habitability of our cases depends on pCO_2, with higher pCO_2 leading to warmer surfaces, due to the greenhouse effect of CO_2 and H_2O

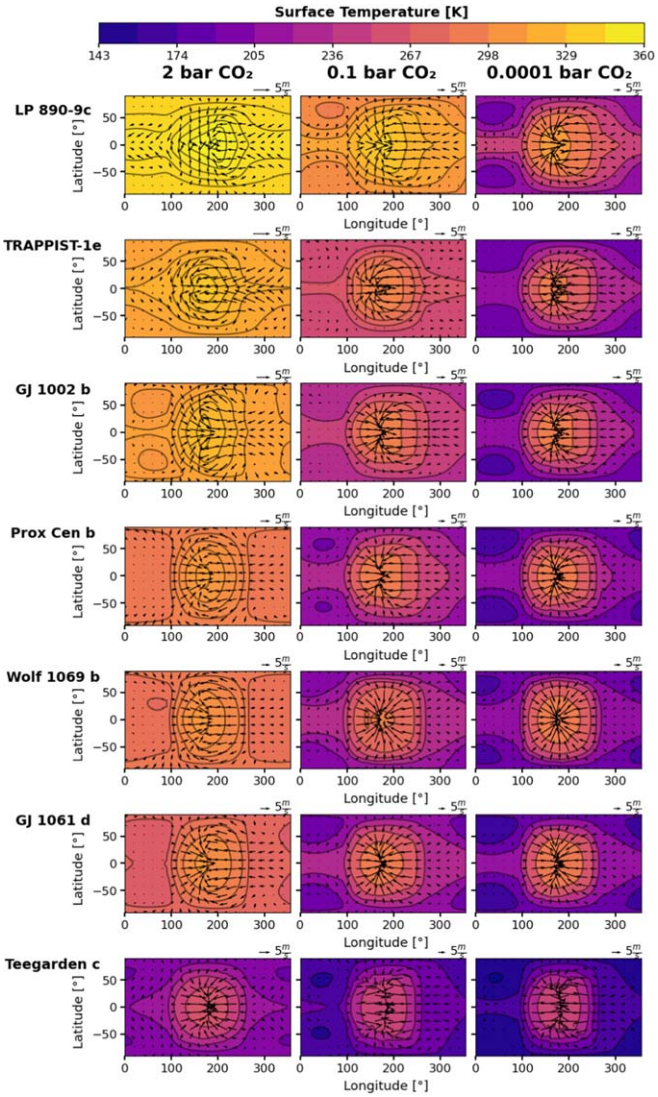

Figure 1. Maps of surface temperature (colors) for each GCM case, for each of our seven considered targets (rows) and varying pCO_2 (columns). Overplotted are the near-surface winds (quivers). The maps are shown as a function of longitude in degrees (x-axis) and latitude in degrees (y-axis), with the substellar point centered at (0°, 0°). All cases share the same color bar for intercomparison. The lighter colors (yellow) represent higher temperatures, while the darker colors (blue) represent lower temperatures. As expected, we find that higher pCO_2 leads to warmer surfaces. All planet cases except Teegarden's Star c have some habitable surface area, with temperatures above the freezing point of water, while Teegarden's Star c is ice-covered for all pCO_2 values considered.

(S. Manabe & R. T. Wetherald 1975). For instance, in the cases of LP 890-9 c, TRAPPIST-1e, and GJ 1002 b, the maximum dayside temperature is above the 50°C conservative threshold for habitability (A. L. Shields et al. 2016; A. H. Lobo et al. 2023; A. H. Lobo & A. L. Shields 2024) in high-pCO_2 cases but below this limit with lower values of pCO_2. However, we find that for all of the pCO_2 cases considered, each of the seven temperate rocky planets considered retains a stable climate below the runaway greenhouse limit. The only exception to our targets having habitable conditions somewhere in our range of considered pCO_2 is the case of Teegarden's Star c, which has temperatures below the freezing point of water everywhere on its surface for all atmospheric compositions that we consider.

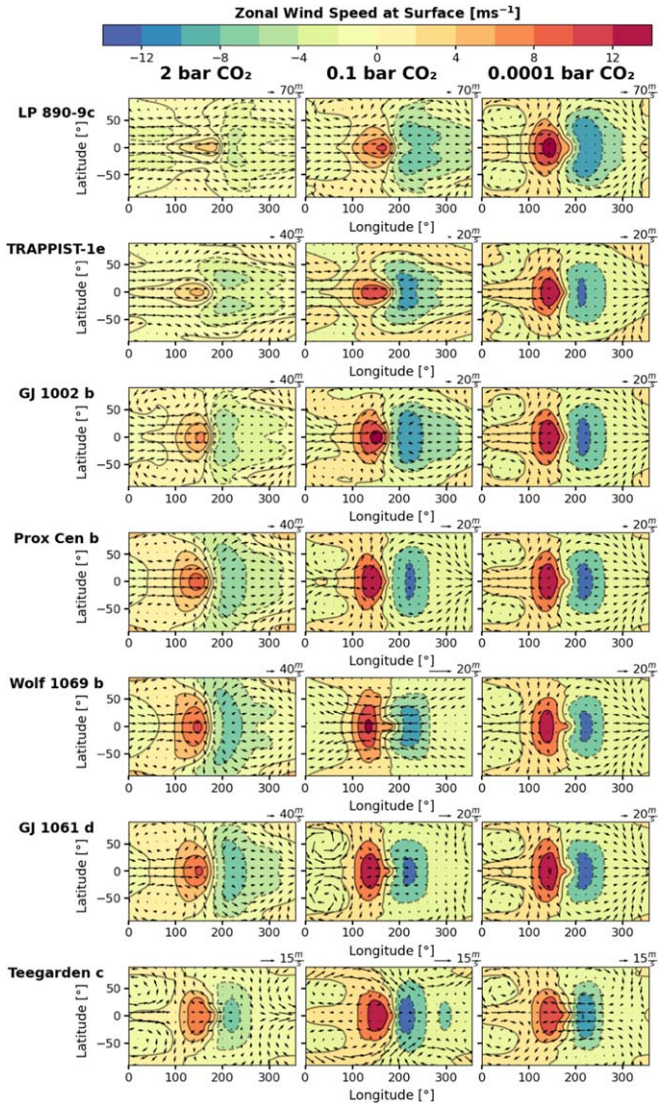

Figure 2. Maps of normalized near-surface zonal wind speed (colors) with directional wind vectors at 250 mbar (quivers) for each GCM case. The quiver magnitudes are normalized separately for each plot. The red shading represents positive zonal wind speeds, while blue represents negative zonal wind speeds. All cases considered have a super-rotating equatorial jet with a maximum wind speed near the western terminator. We find that wind speeds are generally faster for cases with lower pCO_2, driven by the larger day-to-night temperature contrasts (R. Pierrehumbert & M. Hammond 2019) in our cooler cases. However, winds aloft are generally faster in cases with higher instellation and higher pCO_2, with faster super-rotating jets aloft.

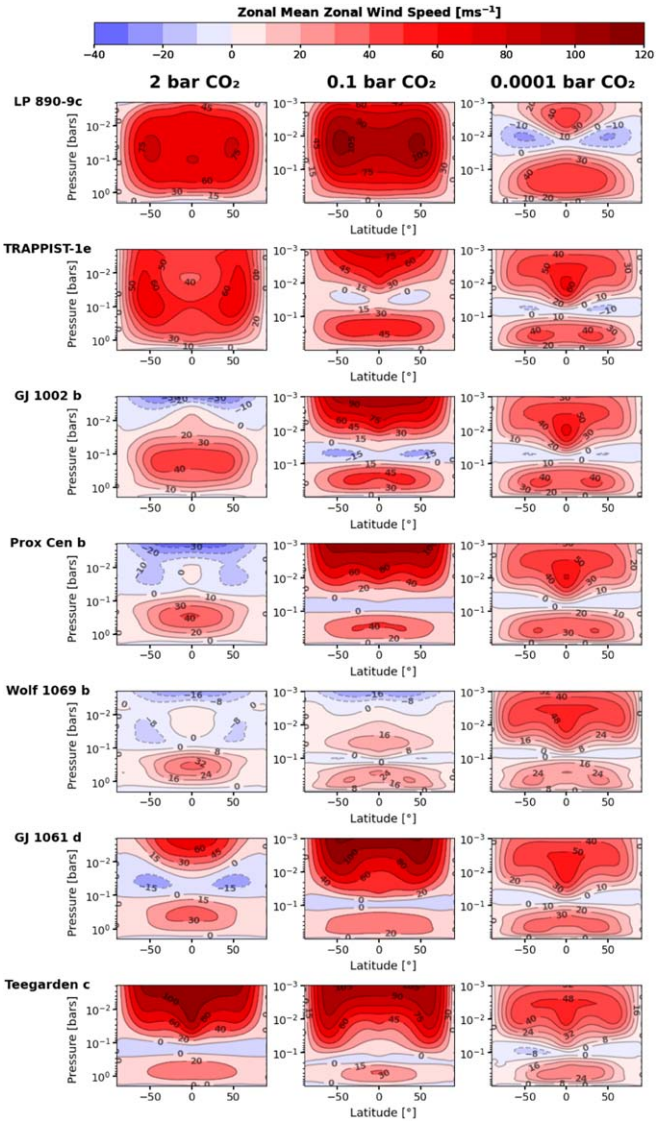

Figure 3. Zonal mean zonal wind (i.e., east–west average of the eastward wind, over all longitudes for a given latitude and pressure), from all planet cases with varying pCO_2. The *y*-axis shows the pressure in bars, and the *x*-axis shows the latitude in degrees. All plots share a color bar. We find that all cases exhibit a super-rotating jet, and we typically find faster jets in cases with intermediate pCO_2.

Figure 2 shows the corresponding near-surface zonal wind speeds (filled and open contours) and 250 mbar winds (quivers) for the 21 simulations of targets at various pCO_2 values. As before, all subplots share a color bar, to assist with intercomparison, but the quiver magnitudes are normalized separately for each plot. In addition, Figure 3 shows the corresponding zonal mean zonal wind from all simulations.

We expect that all cases exhibit dayside convergence as well as atmospheric super-rotation at some pressure level, due to their slow rotation, given that we assume that each planet is tidally locked (A. Showman et al. 2013; R. Pierrehumbert & M. Hammond 2019). The strength of this super-rotating jet increases from the dayside to the nightside, with the fastest wind speeds typically found on the nightside, just west of the western terminator, equatorward of the Rossby lows of the planetary scale Matsuno–Gill pattern (M. Hammond & R. Pierrehumbert 2018). We find that the near-surface circulation is stronger for lower values of pCO_2, likely due to the larger day-to-night temperature contrasts in these cases, with lower global abundances of atmospheric water vapor (J. Haqq-Misra et al. 2018). However, we do not find a clear dependence of circulation strength on instellation, given that the effects of instellation increasing the day-to-night forcing (M. Hammond et al. 2020) and the enhanced moisture leading to latent heat that reduces the day-to-night contrast (M. Labonté & T. Merlis 2020) offset one another. Future work is required to develop a comprehensive theory that incorporates the effects of moisture on the day–night forcing strength and jet speeds of tidally locked planets.

3.1.2. Dynamical Regimes

J. Haqq-Misra et al. (2018) classified the dynamical regimes of tidally locked temperate terrestrial exoplanets into three

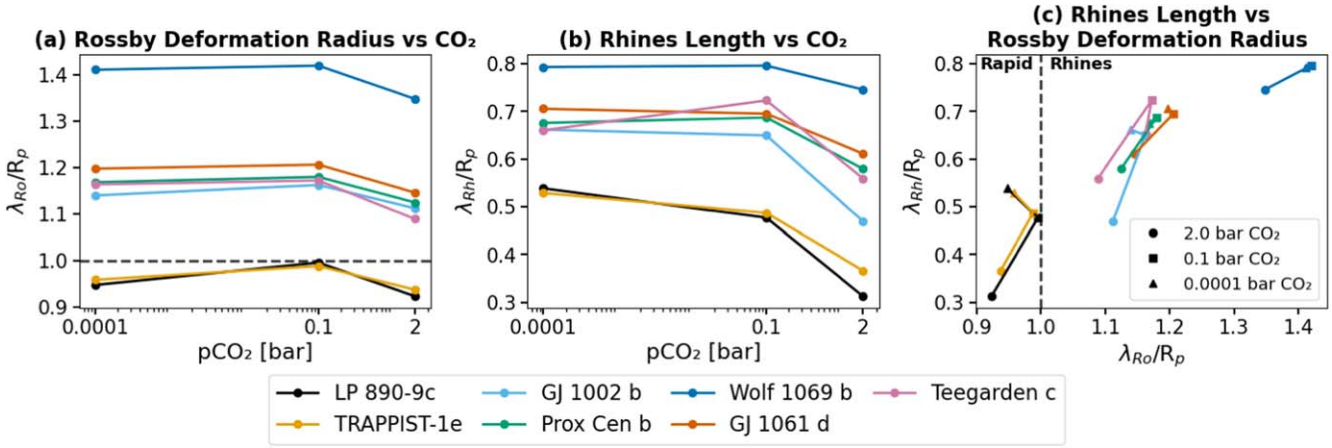

Figure 4. Plots of (a) nondimensional Rossby deformation radius ($\lambda_{\rm Ro}/R_p$) vs. pCO_2, (b) nondimensional Rhines length ($\lambda_{\rm Rh}/R_p$) vs. pCO_2, and (c) nondimensional Rhines length vs. nondimensional Rossby deformation radius, for each planet case. Rapid rotators are defined when $\lambda_{\rm Rh}/R_p < 1$ and $\lambda_{\rm Ro}/R_p < 1$. Rhines rotators are defined when $\lambda_{\rm Rh}/R_p < 1$ and $\lambda_{\rm Ro}/R_p > 1$. Here, only the two highest-irradiation planet cases considered (LP 890-9 c and TRAPPIST-1e) are within the rapid rotator regime regardless of pCO_2, while all other cases are in the Rhines rotator regime.

categories, depending on the ratio of both the Rhines scale and equatorial Rossby deformation radius to the planetary radius (for alternate dynamical regime definitions, see S. Noda et al. 2017; Y. Wang et al. 2018). The equatorial Rossby deformation radius represents the typical meridional length scale at which near-equatorial gravity waves can propagate before being deflected by the Coriolis force, and it can be expressed as

$$\lambda_{\rm Ro} = \sqrt{\frac{R_p\sqrt{gH}}{4\Omega}}. \quad (1)$$

In Equation (1), R_p is the planetary radius, g is the surface gravity, $H = RT/g$ is the scale height, and Ω is the rotation rate. The Rhines scale is the meridional scale at which turbulence manifests into zonal jets. The Rhines scale can be estimated as (P. Rhines 1975)

$$\lambda_{\rm Rh} = \pi\sqrt{\frac{R_p U}{2\Omega}}, \quad (2)$$

where U is the characteristic zonal wind speed.

J. Haqq-Misra et al. (2018) found that temperate planets that orbit later-type host stars are more likely to be in the rapid or Rhines rotator regimes, due to their shorter-period orbits and thus faster rotation rates. Figure 4 shows our predicted dynamical regimes from all 21 simulations of nearby rocky planets with varying pCO_2, showing the individual dependencies of the Rossby deformation radius and Rhines length with CO_2 for each planet, as well as the relationship between them.

We find that all of our simulated targets lie either in the rapid or Rhines rotator regimes. This is likely because these targets were chosen for their high signal-to-noise ratio (SNR) with PIE and typically orbit late-type M dwarf host stars (see Table 1). We predict that the two highest-irradiation targets in our sample, LP 890-9 c and TRAPPIST-1e, lie in the rapid rotator regime for all pCO_2 considered, while all other targets lie in the Rhines rotator regime. Note that TRAPPIST-1e lies at the border of the Rhines and rapid rotator regimes, and the resulting circulation regime depends on the initial conditions and convection parameterization (D. Sergeev et al. 2020, 2022), resulting in differences in circulation regimes between GCMs (D. E. Sergeev et al. 2022).

3.1.3. Cloud Coverage

Because cloud coverage controls the thermal emission of temperate rocky planets (J. Yang et al. 2013, 2014) and is shaped by dynamics on a range of scales (D. Sergeev et al. 2020), we next show the total vertically integrated cloud water path in Figure 5. We find that planet cases with higher instellation and higher pCO_2 typically have a greater global extent of the cloud water path or a higher density of clouds. This is because cold-start cases with low instellation and low pCO_2 only have clouds concentrated near the substellar point, due to the "eyeball" pattern of the open ocean (R. Pierrehumbert 2011). Note that if we instead used a hot start, as in M. Turbet et al. (2021, 2023), the cloud distribution could be vastly different and instead comprised of nightside clouds and a cloud-free dayside, due to the water-vapor feedback.

There is a slight shift of the cloud pattern eastward of the substellar point, due to the predominantly eastward near-equatorial flows transporting clouds lofted near the substellar point downwind. However, we do not include ocean dynamics in these models, which could induce a greater zonal offset in peak ocean temperatures and thus cloud coverage in our moderate-to-low pCO_2 cases assuming an aquaplanet surface (Y. Hu & J. Yang 2014). We find that the case of Teegarden's Star c is an outlier in the total cloud water path, given that the surface is ice-covered and the total atmospheric water-vapor content is much smaller than the other six planet cases.

3.1.4. Bolometric Top-of-atmosphere Thermal Emission

We next turn to consider the impacts of our simulated climate on the top-of-atmosphere outgoing longwave radiation (OLR) that can be probed via phase curves and thermal emission spectroscopy. First, we show spatial maps of the bolometric top-of-atmosphere OLR from our 21 ExoCAM GCM cases in Figure 6. As expected, we find that the total top-of-atmosphere OLR increases with increasing instellation, as required to maintain the planetary energy balance. We further find that the pattern of the top-of-atmosphere OLR is anticorrelated with the cloud water path, as expected, due to the cool cloud tops reducing the thermal emission to space via the cloud greenhouse effect (J. Seeley et al. 2019). This means that the top-of-atmosphere OLR typically peaks westward of

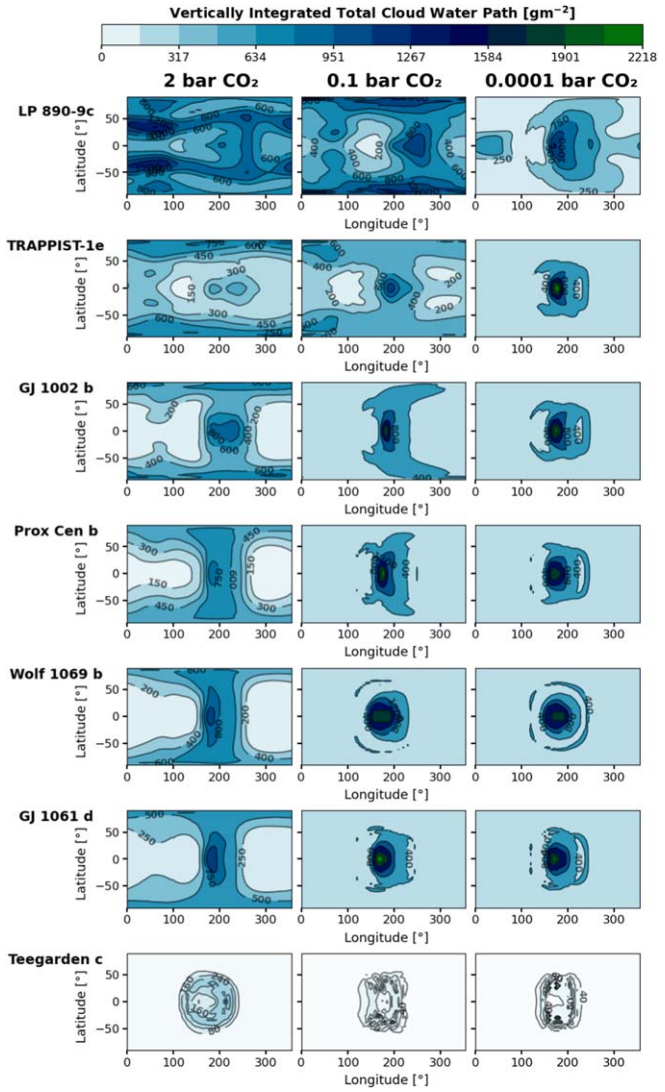

Figure 5. Maps of the vertically integrated total cloud water path (colors) for each GCM simulation. All cases share the same color bar. The darker colors represent areas of higher column water mass, or more total ice and liquid cloud coverage. The hotter cases are generally cloudier, as expected from Clausius–Clapeyron, and they also tend to have lower day–night cloud-coverage contrast, due to their lower day-to-night temperature contrasts (see Figure 1). For most cases, the cloud coverage peaks just eastward of the substellar point, due to the advection of convectively generated clouds near the substellar point by the super-rotating equatorial jet.

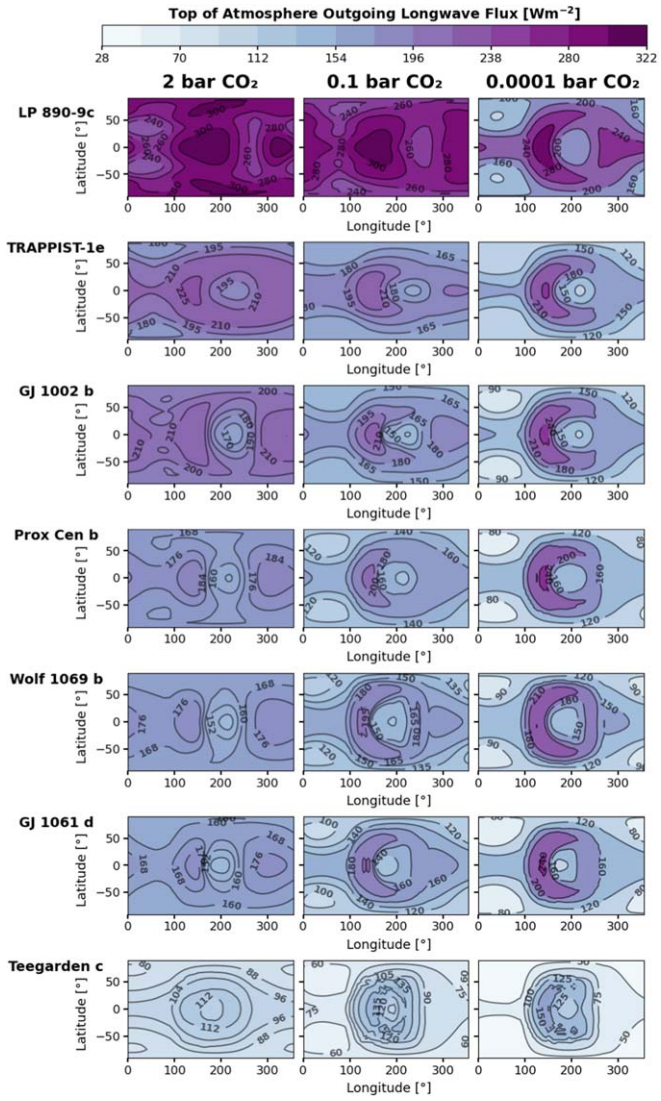

Figure 6. Maps of top-of-atmosphere OLR (colors) for each GCM simulation. All cases share one color bar. The darker (purple) colors represent areas of greater IR (longwave and thermal) emission. Cases with higher overall surface temperatures emit more overall thermal emission to space. Thermal emission to space generally peaks westward of the substellar point, since this is where cloud coverage is lowest.

the substellar point (J. Yang et al. 2013), especially in cases with moderate and low (0.1 bar and 100 μbar) pCO_2. This is because of the super-rotating eastward equatorial jet that blows the peak of the cloud water path eastward of the substellar point, leading to a deficit of clouds on the western dayside and greater surface thermal emission reaching space.

In reality, planets are observed as point sources, with the strongly spatially dependent top-of-atmosphere OLR observed as a hemisphere average. We show such simulated orbital phase curves of bolometric thermal emission from our ExoCAM GCMs in Figure 7. Note that each panel has a different y-axis scale. We calculate the phase curves as in N. Cowan & E. Agol (2008), integrating the global OLR at each latitude and longitude, taking into account the viewing angle to obtain the total OLR for each hemisphere. Each phase curve for a given target and value of pCO_2 is normalized to its mean value, in order to facilitate intercomparison, and the phase curves are plotted as a function of the subobserver longitude (rather than, e.g., the orbital phase), assuming that the hemisphere the observer sees is centered on the equator—however, note that many of these planets are nontransiting, and thus the subobserver latitude is a priori unknown (E. Rauscher 2017). As expected, we find that typically cases with moderate instellation and $pCO_2 \lesssim 0.1$ bar have phase curves that peak westward of the substellar point, due to the eastward shift in the maximum cloud coverage (J. Yang et al. 2013; T. Komacek & D. Abbot 2019). However, we find that cases with high pCO_2 and the hottest planet case (LP 890-9c) exhibit more complex phase curves that can have multiple peaks, typically one westward of the substellar point and one on the nightside, eastward of the eastern limb. Meanwhile, the coolest planet that we simulated (Teegarden's Star c) has thermal emission maxima either near the substellar point or slightly eastward of it, due to the reduced impact of cloud coverage on thermal

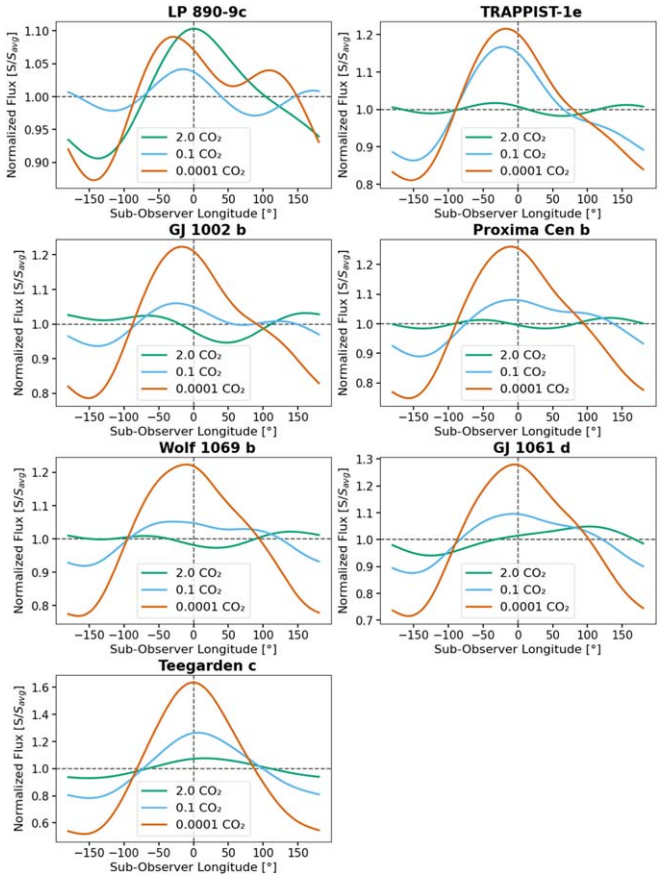

Figure 7. The normalized broadband thermal phase curves for all three pCO_2 cases, for each planet simulated with ExoCAM. These bolometric phase curves are calculated from the ExoCAM radiative transfer output outgoing longwave radiation at the top of atmosphere summed over wavelength. Each phase curve is normalized to its own average value, in order to compare the relative phase-curve amplitudes between planets and with varying pCO_2. Note that each plot has a different y-axis scaling, with Teegarden's Star c having a much larger phase-curve amplitude than LP 890-9 c. As in J. Haqq-Misra et al. (2018), we find that phase-curve amplitudes increase with decreasing planetary temperature, due to the limited effect of the water latent heat on heat transport.

emission in this case. As a result, Teegarden's Star c shows the largest phase amplitude, given the significant difference in cloud cover and resulting OLR between the dayside and nightside. In contrast, LP 890-9 c has the smallest phase-curve amplitude, reflecting its relatively spatially uniform OLR, due to the high moisture content leading to efficient day-to-night heat transport (J. Haqq-Misra et al. 2018; M. Labonté & T. Merlis 2020).

3.2. PSG Post-Processing

We next turn to our results from the PSG post-processing of our 21 ExoCAM GCMs for varying targets and pCO_2, in order to determine the detectability of spectral features in the MIR using a MIRECLE-like mission with the PIE technique.

3.2.1. Thermal Emission Spectra with PIE

In Figure 8, we plot the thermal emission spectra at 270° phase for varying pCO_2 alongside vertical profiles of the total cloud water path and temperature, for each target considered.

We find that all cases have a distinguishable CO_2 feature at 15 μm, and most have water features centered at 6.2 and 7.3 μm. Figure 9 shows the same set of spectra for each planet and pCO_2 including clouds, now compared with cloud-free counterparts simulated using PSG, solely removing the impact of liquid and ice clouds but assuming that the climate is unchanged. We find that hotter cases with resulting high-altitude clouds, most notably LP 890-9 c, generally have weaker spectral features.

This is because these high-altitude clouds absorb and re-radiate outgoing longwave radiation originating from deeper in the atmosphere, decreasing the flux level of the continuum and thus decreasing the strength of the absorption features. Similarly, we find that these cases with high-altitude (low-pressure) maxima in the cloud water path have significantly muted water-vapor spectral features. Conversely, we find that cooler targets with reduced cloud cover (e.g., Teegarden's Star c) have a smaller impact of clouds on the resulting spectra.

We also find that the shape of the 15 μm CO_2 feature is strongly dependent on pCO_2 itself, with higher-pCO_2 cases having broader CO_2 features. This is due largely to pressure broadening with increasing pCO_2, which in some cases is affected by overlap between neighboring H_2O and CO_2 features in these hot and moist atmospheres with high pCO_2 (D. D. B. Koll et al. 2023). In addition, the 15 μm CO_2 feature in some of our hottest cases (e.g., LP 890-9 c with $pCO_2 = 2$ bars) has a markedly different shape and lower amplitude. This is likely due to a slight thermal inversion in the upper atmosphere that is driven by water-vapor absorption (given that our ExoCAM models have no O_3), increasing the outgoing top-of-atmosphere flux from within the CO_2 band.

In reality, MIRECLE will be observing targets at distinct phases of the planet's orbit. We compute spectra at four phases: 0°, 90°, 180°, and 270°, which correspond to observing hemispheres centered on the dayside, eastern limb, nightside, and western limb, respectively. For most cases, the observed flux on the dayside is generally lower than the observed nightside flux, due to high dayside cloud cover, except for the flux at the 15 μm CO_2 feature in cases with 2 bars of CO_2, which occurs as an emission rather than absorption feature on the dayside in our hottest cases considered. Notably, this 15 μm feature on the dayside of LP 890-9 c is very strong, due to the high amount of OLR emitted on the dayside (see Figure 6). Conversely, the observed dayside of Teegarden's Star c has much larger relative flux, because the planet is so cold, and as a result there are fewer clouds to absorb and re-radiate outgoing flux from the surface.

3.2.2. Detectability of CO_2 with MIRECLE

We now use our simulated spectra shown in Figure 8 to quantify the detectability of CO_2 in nearby temperate rocky planet atmospheres. We choose CO_2 because it has the highest feature amplitude and because constraining the abundance of CO_2 on many exoplanet atmospheres could provide an inference about the feasibility of the habitable zone hypothesis (J. Bean et al. 2017; O. R. Lehmer et al. 2020; J. H. Checlair et al. 2021). We calculate the molecular SNR as (J. Lustig-Yaeger et al. 2019; Y. Rotman et al. 2023)

$$\mathrm{SNR} = \sqrt{\sum_{\lambda}\left(\frac{F_{\lambda,\mathrm{CO_2}} - F_{\lambda,\mathrm{noCO_2}}}{\sigma_{\lambda}}\right)^2}, \quad (3)$$

where $F_{\lambda,\mathrm{CO_2}}$ and $F_{\lambda,\mathrm{noCO_2}}$ are the wavelength-dependent planetary thermal fluxes in simulations with and without

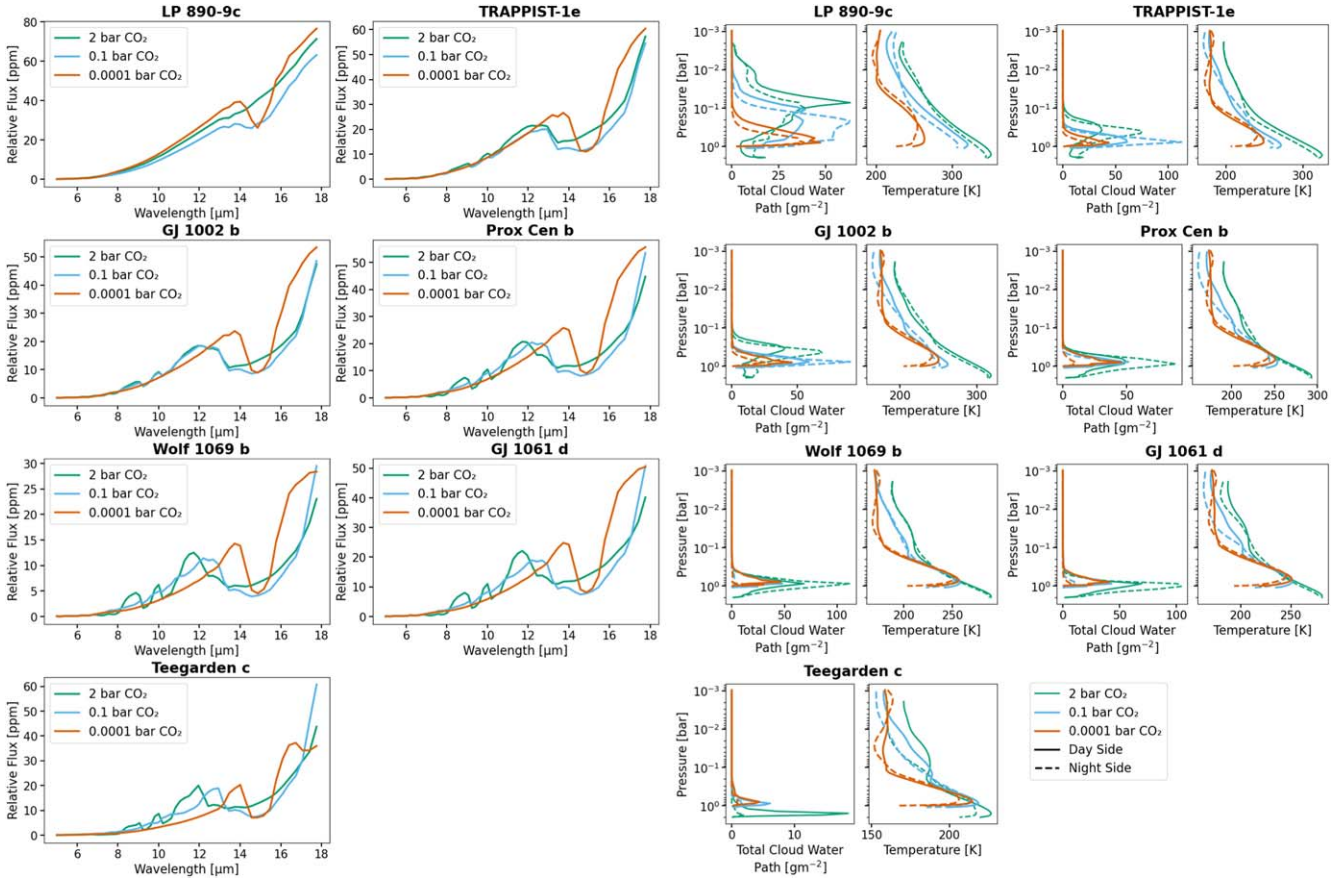

Figure 8. Modeled PSG emission spectra (left-hand panels) and ExoCAM vertical profiles of cloud coverage and temperature (right-hand panels), averaged over the dayside (solid lines) and nightside (dashed lines), for each planet and pCO_2 case (colors). For most cases, there is a prominent absorption feature of CO_2 at 15 μm, as well as water-vapor features. We find that cases with higher instellation have reduced water and carbon dioxide feature strengths, due to the presence of a greater cloud water path at low pressures.

including CO_2 in the PSG post-processing, and σ_λ is the wavelength-dependent noise from the PSG noise calculator.

Figure 10 shows the simulated spectra for each case at the four different phases considered, while Figure 11 shows the molecular SNR for CO_2 for each of our targets and considered pCO_2 cases, assuming 30 days of observation with MIRECLE.

Figure 12 shows the SNR calculated at each phase. Note that the 0° and 180° cases are adjusted to 2° and 182°, respectively, to account for transits and secondary eclipses, given that some of our considered targets are transiting.

Finally, Figure 13 shows the SNR calculated for a range of exposure times and two telescope diameters. Note that 1.5 m is our default telescope diameter for all previous simulations.

We find that the SNR for CO_2 given 30 days of observation with MIRECLE is always greater than 5 for three planet targets, regardless of pCO_2: Proxima Centauri b, GJ 1061 d, and GJ 1002 b. We also find that if $pCO_2 \gtrsim 0.1$ bar, CO_2 may be detectable on Teegarden's Star c. Clouds have little impact on the SNR at 15 μm, as the CO_2 is expected to be well mixed above the cloud deck. Phase, however, can influence detectability, particularly for cold planets (e.g., Teegarden's Star c), given their large predicted day-to-night temperature contrast, as well as hotter planets (e.g., LP 890-9c), at intermediate values of pCO_2, due to strong day-to-night cloud-coverage variations. In general, it is worthwhile to observe a planet with PIE at multiple phases, both in order to better build up the SNR as well as to infer significant day–night differences that could provide additional constraints on the planetary climate.

Note that the key effect in our SNR calculation is distance from the system, as all three systems that we confidently predict would have detectable pCO_2 given an otherwise Earth-like atmosphere are nearby, with separations $\leqslant$4.8 pc. The only exception to this is for very cold planets, as Teegarden's Star is $\sim$1 pc closer than GJ 1002, but the SNR of Teegarden's Star c is much lower than GJ 1002 b for $pCO_2 \lesssim 0.1$ bar. Thus, MIRECLE is well suited to studying the thermal emission of temperate rocky planets via PIE for sufficiently nearby targets, with Proxima Centauri b serving as a best-case scenario.

4. Discussion

4.1. Implications for Characterization of Temperate Rocky Planets in Thermal Emission

We find from our suite of ExoCAM GCMs and PSG radiative transfer post-processing that the climates of temperate rocky exoplanets play a key role in their potential to be characterized in thermal emission with the PIE technique. Our cases with higher instellation have a higher surface temperature, leading to a greater amount of atmospheric water vapor and thus a higher overall cloud coverage and a reduced day-to-night temperature contrast (J. Yang et al. 2013; J. Haqq-Misra et al. 2018; M. Labonté & T. Merlis 2020).

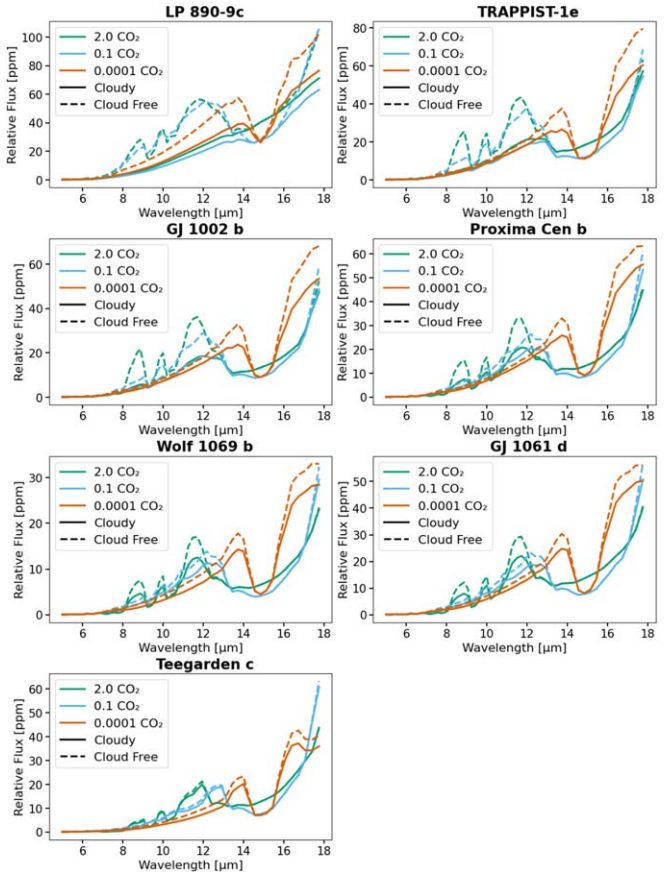

Figure 9. Modeled PSG emission cloudy (solid lines) and cloud-free (dashed lines) spectra for each planet and pCO_2 case (colors). The cloud-free cases represent PSG GlobES runs with no aerosol absorption. The effect of clouds on the thermal spectra is generally the highest for warm planets with a thick cloud deck. Reduced cloudiness allows for outgoing thermal emission to radiate out of the deeper atmosphere and not be absorbed and re-emitted by optically thick clouds.

Notably, at higher surface temperatures (due to high instellations and/or high pCO_2), the cloud deck moves upward to higher altitudes. These higher-altitude cloud decks absorb and re-emit thermal radiation, reducing the flux of the continuum and thus reducing the amplitude of the spectral features of key molecular rovibrational bands. Thus, clouds can hamper detections of molecular features in thermal emission, but not to as great an extent as transmission, given the larger optical path in that case (J. J. Fortney 2005; T. J. Fauchez et al. 2019; G. Suissa et al. 2020a). In addition, cooler cases have a reduced amount of opaque high-altitude clouds but at the expense of a reduced thermal flux, implying a smaller signal with the PIE technique. As a result, detections of spectral features in the MIR with PIE are likely most feasible for planets that are sufficiently hot to have high thermal flux while cool or dry enough to prevent the formation of opaque high-altitude cloud decks.

The day–night variation in our simulations provides crucial insight into the climate and rotational dynamics of the observed planet. These flux variations can be influenced by the rotation rate (J. Haqq-Misra et al. 2018; R. Pierrehumbert & M. Hammond 2019), atmospheric composition, specifically greenhouse gases (M. Turbet et al. 2016; E. Wolf 2017), which further shape global and vertical temperature patterns, and cloud/haze coverage (J. Yang et al. 2013; T. J. Fauchez et al. 2019). Therefore, observations at multiple phases could provide valuable constraints on a planet's rotation rate and determine if a given planet has a stable climate or if it exhibits a runaway greenhouse state.

4.2. Relevance to Venus and Its Analogs

The simulations provided in this work have demonstrated the potential detectability of CO_2 at 15 μm. The presence of atmospheric CO_2 is expected in a variety of terrestrial planet evolution scenarios that, in extreme cases, can result in a thick CO_2-dominated atmosphere. The detection of such a scenario may enable the characterization of the evolutionary state of the planet as having entered a post-runaway greenhouse phase, similar to that of present-day Venus. Identifying the major factors that caused Venus' climate to diverge so drastically from that of Earth is paramount for understanding the evolutionary pathways of terrestrial planets and the formation of habitable worlds (S. R. Kane et al. 2019; S. R. Kane & P. K. Byrne 2024). The study of exoplanets in the Venus Zone, or exoVenuses, is a complementary pathway to learning about Venus and its history (S. R. Kane et al. 2014, 2018; C. Ostberg & S. R. Kane 2019; S. R. Kane 2022; C. Ostberg et al. 2023b). Indeed, the further study and understanding of the evolution of Venus' atmosphere and its present state provides a foundation of planetary habitability on which the interpretation of exoplanet observations depends (S. R. Kane et al. 2021).

Exoplanet models are "ground-truthed" through analyses of atmospheric data for our sibling planet, such as those that will be provided by the coming deployment of the Deep Atmosphere Venus Investigation of Noble gases, Chemistry, and Imaging, designed to accurately measure the pressure, temperature, composition, and chemistry of the Venus atmosphere all the way down to the surface (J. B. Garvin et al. 2022). Current transmission spectroscopy methods, and the interpretation of those data, are limited by the relatively high atmospheric scale height of those measurements and the presence of hazes, making it difficult to effectively distinguish between Venus- and Earth-analog atmospheres (D. Ehrenreich et al. 2012; J. K. Barstow et al. 2016; J. Lustig-Yaeger et al. 2019; C. Ostberg et al. 2023a). For example, JWST has provided the opportunity to study the atmospheres of potential exoVenuses, including TRAPPIST-1 b and c, the results of which are consistent with little to no atmosphere (T. P. Greene et al. 2023; S. Zieba et al. 2023). The emission spectra described in this work would yield important diagnostics that could significantly reduce the ambiguity between temperate and post-runaway greenhouse scenarios for nearby rocky planets in the habitable zone.

4.3. Limitations

Our modeling framework was simplified in order to serve as an exploration of the effects of 3D climate properties on the thermal emission of nearby rocky exoplanets as observed with the PIE technique, across a diverse selection of exoplanets. As a result, we made a variety of necessary simplifying assumptions regarding the system and planetary properties, observation geometry, and atmospheric composition and variability.

First, we assumed that all of the planet targets we studied were tidally locked to their host star, with a 1:1 spin–orbit ratio. Though this is well motivated through short spin-synchronization timescales for such close-in orbits, it is not known if these

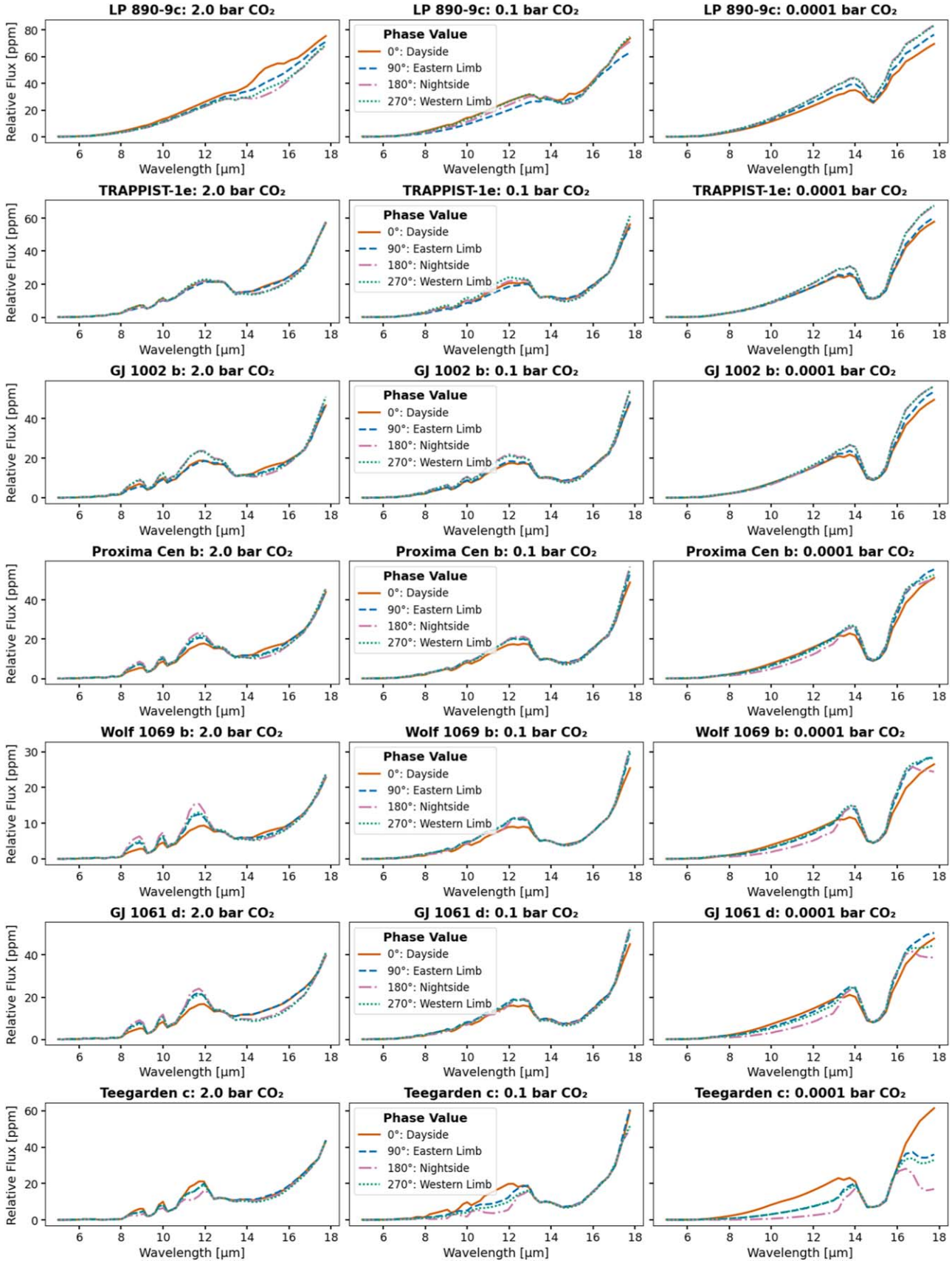

Figure 10. Modeled PSG emission spectra at four phases (colors and line styles) for each planet and pCO_2 case. Especially for planets with reduced instellation (where rows are ordered with decreasing instellation, from top to bottom), the water features when observing the dayside have lower in-band fluxes than when observing the nightside, except for Teegarden's Star c. For the 2 bar CO_2 cases, the flux in the line core of the 15 μm CO_2 feature observed on the dayside is typically higher than that on the nightside.

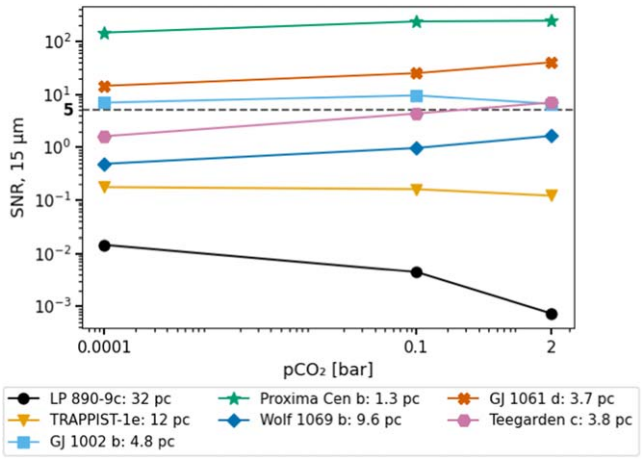

Figure 11. The calculated molecular SNR for each model case at 15 μm for 30 days of observation with MIRECLE. CO_2 in the atmospheres of cases above the noise floor (5 ppm) is more likely to be detected by the MIRECLE telescope with our chosen instrumental parameters. In general, temperate planets within ∼5 pc are the best targets for potentially detecting CO_2.

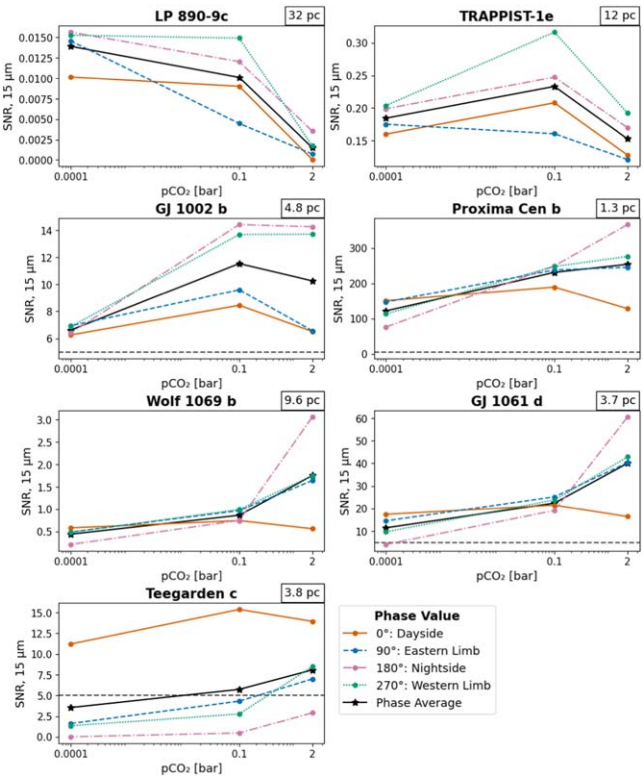

Figure 12. The calculated molecular SNR at four phase values (the colors and line styles are the same as in Figure 10) for each model case at 15 μm, given 30 days of observation with MIRECLE. The black line with star markers represents the SNR averaged over all phases. For all cases except Teegarden's Star c, the phased averaged SNR is less than that at 270° alone—the phase set in Figures 8 and 11.

targets are indeed tidally locked. For instance, TRAPPIST-1e may or may not have a nonzero obliquity (N. Guerrero & S. Ballard 2024; S. C. Millholland et al. 2024), and in general the spins of planets in close-in compact near-resonant systems may be chaotic and lead to strongly time-dependent atmospheric circulation (H. Chen et al. 2023). In addition, it is plausible that close-in planets without known companions are in a 3:2 rather than a 1:1 spin–orbit resonance, leading to

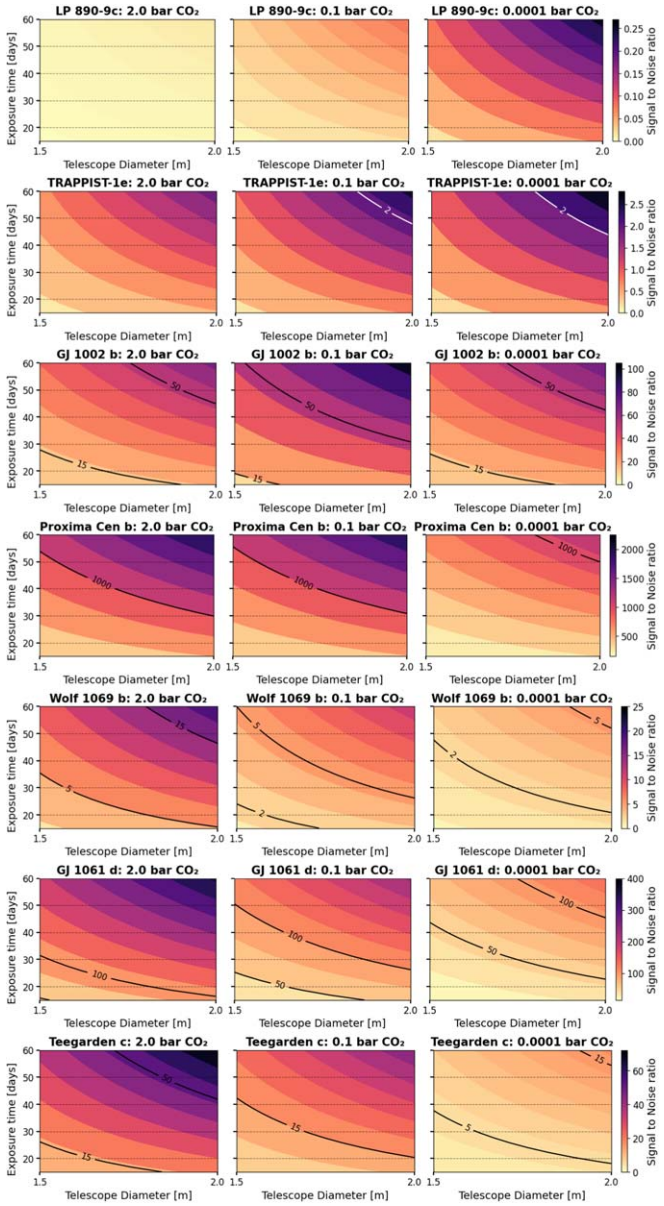

Figure 13. The calculated molecular SNR (colors and contour lines) given varying exposure times and MIRECLE telescope diameters for each model case at 15 μm. Each row uses a different color bar range, so as to compare cases with varying CO_2 for a given planet to one another. We find that the SNR increases with increasing exposure time and telescope diameter, as expected. With about 10 days more exposure time, the 2 bar CO_2 case for Wolf 1069 b would be within our 5 SNR limit for detectability. Meanwhile, we find that the 15 μm CO_2 feature will likely not be detectable on LP 890-9 c and TRAPPIST-1e within a reasonable exposure time given a 1.5 meter - 2 meter telescope diameter.

significant differences in their simulated climate states (M. Turbet et al. 2016).

A key limitation of this work is that the radii of nontransiting planets are unknown, and only the minimum mass is formally constrained. As a result, here we chose radii and surface gravities from the literature that assume a broadly Earth-like interior composition, but it is feasible that specific targets will have a different composition than expected, based on population-level mass–radius relationships (e.g., J. Chen & D. Kipping 2017), requiring GCMs to formally consider a range of radii surface gravities. It is also feasible that the actual

planet masses are significantly larger than the minimum mass, as used in this study.

Our simulated observations were simplistic, in that we only considered one inclination and one planetary phase for all observations. All observations assumed a 90° inclination, but if the system is more inclined, the planetary thermal emission signal will decrease, due to a greater hemispheric contribution from the colder poles. As a result, we anticipate that the predictions presented here are upper limits for the detectability of CO_2 of these targets with PIE. In addition, PSG uses R. L. Kurucz (2005) stellar templates for all spectra calculations. However, in reality, M dwarf stars are variable, and true spectral models can complicate the interpretation of planetary spectral features, especially those that also appear in the stellar photosphere.

We neglected the potential time variability of the atmospheric circulation of these planets in our post-processing of GCM simulations. This variability in cloud and water-vapor distributions has been shown to have a ∼10 ppm level impact on the transmission spectra of TRAPPIST-1e (E. May et al. 2021; T. J. Fauchez et al. 2022; Y. Rotman et al. 2023), with ExoCAM showing the highest amplitude and longest periodicity of variability out of the four GCMs included. We neglected ocean dynamics in our ExoCAM GCM simulations, which would affect the surface temperature distribution and potentially impact the resulting cloud patterns and top-of-atmosphere OLR (Y. Hu & J. Yang 2014; A. Salazar et al. 2020; K. Batra & S. L. Olson 2024). We also neglected the potential impact of photochemistry on atmospheric composition (H. Chen et al. 2021; M. Braam et al. 2023), especially any time-dependent photochemistry and atmospheric loss due to the high flaring activities of these late-type stars (L. N. R. do Amaral et al. 2022; J. N. Ealy et al. 2024; E. F. Fromont et al. 2024). Future work is required to quantify whether time-dependent atmospheric chemistry could be detectable in thermal emission with MIRECLE and/or LIFE.

4.4. Future Work

Our preliminary study considering seven nearby targets with a terrestrial planet GCM is promising, in that we find that key molecular features may be detectable with PIE using a MIRECLE-like observatory. However, the limitations of this work described above motivate significant follow-up work to explore the broad range of potential planetary properties, atmospheric compositions, and observing geometries.

One key constraint regarding the atmospheric composition is that it does not take into account photochemistry, especially haze formation in methane-rich atmospheres (G. Arney et al. 2016, 2017). Recent work has shown that haze formation due to methane photodissociation on TRAPPIST-1e can significantly impact the planetary climate (M. T. Mak et al. 2024). Notably, M. T. Mak et al. (2024) found that hazes could either cool or warm the underlying atmosphere, depending on the ratio of pCO_2 to pCH_4. Future work is needed to couple a 3D GCM and a 1D photochemistry model for simulations of nearby nontransiting rocky planet targets, in order to make predictions for the resulting methane and haze profiles and their impact on climate and observable properties.

At the time of this study, ExoCAM does not natively include oxygen and ozone, yet they have features in the MIR (T. J. Fauchez et al. 2020). Separate work is already underway to formally include absorption oxygen species and associate collision-induced absorption (R. Deitrick et al. 2025, in preparation). In addition, the 3D ozone distribution on tidally locked planets is dynamic, with ozone preferentially accumulated in the cool Rossby gyres on the nightside and limb (M. Braam et al. 2023). Thus, future work is required to include both methane and ozone photochemistry in ExoCAM, in order to make detailed predictions for biosignature detections in the atmospheres of nearby temperate rocky exoplanets.

5. Conclusions

In this work, we have conducted a large suite of 21 GCM simulations of prime nearby habitable zone rocky planet candidates with the ExoCAM GCM for varying assumed atmospheric compositions, varying the partial pressure of carbon dioxide from 100 μbar to 2 bars. We then post-processed these GCM simulations with the PSG to make predictions for the potential observational characterizations of these targets with the PIE technique via thermal emission spectra and phase curves. We summarize our key findings as follows.

1. Out of the seven nearby rocky planet targets we simulated, six can have habitable surface conditions over the range of CO_2 partial pressure that we considered. The only exception is Teegarden's Star c, which has a fully ice-covered surface even at a CO_2 partial pressure of 2 bar. We further find, as expected, that the climate, circulation, and temperature patterns of each target are strongly dependent on the assumed CO_2 partial pressure, with higher CO_2 abundances leading to lower day-to-night temperature contrasts and weaker wind speeds.
2. Our ExoCAM simulations predict extensive water cloud coverage on all six of the targets that have habitable surface conditions. This cloud coverage transitions from being largely confined near the substellar point, at low CO_2 abundances, to extending from pole to pole on the dayside, at higher CO_2 abundances, and even on the nightside for our high-instellation planet cases. As expected, we find that this cloud coverage is anticorrelated with the top-of-atmosphere OLR, leading to a westward shift in the peak of thermal emission, due to the eastward shift of the cloud maximum due to advection by the super-rotating jet.
3. We find that clouds control the phase-dependent thermal emission of our habitable rocky planet targets. Their phase curves peak at subobserver longitudes centered westward of the substellar point, due to the decreased cloud coverage there. In addition, the 15 μm CO_2 feature amplitude is largest in cases with low CO_2 abundances, due to the reduced high cloud cover. Conversely, water-vapor features are stronger in cases with higher CO_2 abundances, due to the enhanced amount of water vapor in the atmosphere.
4. We predict that the PIE technique can enable the detection of carbon dioxide in the atmospheres of nearby habitable zone targets. Specifically, we expect that the 15 μm CO_2 feature is detectable for Proxima Centauri b, GJ 1061 d, and GJ 1002 b, with less than 30 days of observation with a MIRECLE-like observatory for any of the CO_2 partial pressures we considered. In addition, we predict that CO_2 would be detectable on Teegarden's Star c in the same conditions for sufficiently high-CO_2 partial pressures. Future work is needed to determine the detectability of

the range of possible habitability indicators and biosignatures in thermal emission for nearby nontransiting rocky planets with PIE.

Acknowledgments

We thank the referee for the thoughtful report, which improved this work. We thank Kevin Stevenson for helpful discussions regarding PIE. We also thank Stephanie Olson for her support and guidance during the final stages of this project. We acknowledge support from NASA Habitable Worlds Program grant No. 80NSSC24K0215. This material is based upon work performed as part of the CHAMPs (Consortium on Habitability and Atmospheres of M-dwarf Planets) team, supported by the National Aeronautics and Space Administration (NASA) under grant Nos. 80NSSC21K0905 and 80NSSC23K1399, issued through the Interdisciplinary Consortia for Astrobiology Research (ICAR) program. V.K. and R.K. were supported by the GSFC Sellers Exoplanet Environments Collaboration (SEEC), which is supported by the NASA Planetary Science Division's Internal Scientist Funding Model, and Exoplanets Spectroscopy Technologies (ExoSpec), which is a part of the NASA Astrophysics Science Division's Internal Scientist Funding Model. The authors are grateful for the NCCS Discover and University of Maryland Zaratan supercomputing resources (http://hpcc.umd.edu) that enabled this research. All ExoCAM and PSG simulation data is available at doi:10.5281/zenodo.15106452.

Appendix
Global Mean GCM Output

Table 4 shows the global mean simulation output for surface temperature, day–night surface temperature contrast, cloud fraction, shortwave albedo, and top-of-atmosphere upward longwave flux from each planetary case considered in this work.

Table 4
Key Values for Each Model Case Averaged Globally over Latitude and Longitude, as Well as Time-averaged over the Last 10 yr of GCM Output

Planet Name	pCO_2 (bar)	Global Mean T (K)	Day–Night ΔT (K)	Global Cloud Fraction	Global Shortwave Albedo	Global TOA Upward LW (Wm^{-2})
LP 890-9c	2	345	3	0.55	0.58	489
	0.1	313	11	0.80	0.58	369
	0.0001	244	41	0.46	0.61	213
TRAPPIST-1e	2	320	6	0.56	0.58	327
	0.1	265	18	0.49	0.59	209
	0.0001	223	37	0.33	0.70	152
GJ 1002 b	2	315	7	0.52	0.58	310
	0.1	252	23	0.35	0.63	190
	0.0001	221	43	0.33	0.69	151
Proxima Centauri b	2	293	10	0.59	0.58	238
	0.1	237	33	0.28	0.66	169
	0.0001	217	47	0.31	0.68	143
Wolf 1069 b	2	289	11	0.53	0.58	227
	0.1	238	35	0.23	0.63	170
	0.0001	220	48	0.31	0.65	149
GJ 1061 d	2	280	15	0.43	0.52	214
	0.1	230	38	0.26	0.66	157
	0.0001	213	50	0.29	0.68	135
Teegarden's Star c	2	217	28	0.24	0.76	108
	0.1	195	47	0.27	0.77	90
	0.0001	180	47	0.27	0.77	73

ORCID iDs

Tobi Hammond https://orcid.org/0009-0002-5756-9778
Thaddeus D. Komacek https://orcid.org/0000-0002-9258-5311
Ravi K. Kopparapu https://orcid.org/0000-0002-5893-2471
Thomas J. Fauchez https://orcid.org/0000-0002-5967-9631
Avi M. Mandell https://orcid.org/0000-0002-8119-3355
Eric T. Wolf https://orcid.org/0000-0002-7188-1648
Vincent Kofman https://orcid.org/0000-0002-5060-1993
Stephen R. Kane https://orcid.org/0000-0002-7084-0529
Ted M. Johnson https://orcid.org/0000-0002-1570-2203
Anmol Desai https://orcid.org/0009-0000-9206-5589
Giada Arney https://orcid.org/0000-0001-6285-267X
Jaime S. Crouse https://orcid.org/0000-0003-2273-8324

References

Agol, E., Dorn, C., Grimm, S. L., et al. 2021, PSJ, 2, 1
Anglada-Escudé, G., Amado, P., Barnes, J., et al. 2016, Natur, 536, 437
Arney, G., Domagal-Goldman, S. D., Meadows, V. S., et al. 2016, AsBio, 16, 873
Arney, G. N., Meadows, V. S., Domagal-Goldman, S. D., et al. 2017, ApJ, 836, 49
Barstow, J. K., Aigrain, S., Irwin, P. G. J., Kendrew, S., & Fletcher, L. N. 2016, MNRAS, 458, 2657
Batra, K., & Olson, S. L. 2024, ApJL, 971, L11
Bean, J., Abbot, D., & Kempton, E. 2017, ApJL, 841, L24
Bitz, C., Shell, K., Gent, P., et al. 2012, JCli, 25, 3053
Boldog, Á, Dobos, V., Kiss, L. L., van der Perk, M., & Barr, A. C. 2024, A&A, 681, A109
Boutle, I., Mayne, N., Drummond, B., et al. 2017, A&A, 601, A120
Boutle, I. A., Mayne, N. J., Drummond, B., et al. 2017, A&A, 601, A120
Braam, M., Palmer, P. I., Decin, L., Cohen, M., & Mayne, N. J. 2023, MNRAS, 526, 263
Checlair, J. H., Villanueva, G. L., Hayworth, B. P. C., et al. 2021, AJ, 161, 150
Chen, H., Li, G., Paradise, A., & Kopparapu, R. 2023, ApJ, 946, L32
Chen, H., Zhan, Z., Youngblood, A., et al. 2021, NatAs, 5, 298
Chen, J., & Kipping, D. 2017, ApJ, 834, 17
Cowan, N., & Agol, E. 2008, ApJL, 678, L129
De Luca, P., Braam, M., Komacek, T. D., & Hochman, A. 2024, MNRAS, 531, 1471
Del Genio, A., Way, M., Amundsen, D., et al. 2019, AsBio, 19, 1
Delrez, L., Murray, C. A., Pozuelos, F. J., et al. 2022, A&A, 667, A59
do Amaral, L. N. R., Barnes, R., Segura, A., & Luger, R. 2022, ApJ, 928, 12
Dreizler, S., Jeffers, S. V., Rodríguez, E., et al. 2020, MNRAS, 493, 536
Ealy, J. N., Schlieder, J. E., Komacek, T. D., & Gilbert, E. A. 2024, ApJ, 168, 173
Ehrenreich, D., Vidal-Madjar, A., Widemann, T., et al. 2012, A&A, 537, L2
Fauchez, T. J., Turbet, M., Villanueva, G. L., et al. 2019, ApJ, 887, 194
Fauchez, T. J., Villanueva, G. L., Schwieterman, E. W., et al. 2020, NatAs, 4, 372
Fauchez, T. J., Villanueva, G. L., Sergeev, D. E., et al. 2022, PSJ, 3, 213
Fortney, J. J. 2005, MNRAS, 364, 649
Fromont, E. F., Ahlers, J. P., do Amaral, L. N. R., et al. 2024, ApJ, 961, 115
Fujii, Y., Genio, A. D., & Amundsen, D. 2017, ApJ, 848, 100
Garcia, V., Smith, C. M., Chavas, D. R., & Komacek, T. D. 2024, ApJ, 965, 5
Garvin, J. B., Getty, S. A., Arney, G. N., et al. 2022, PSJ, 3, 117
Gilbert, E. A., Vanderburg, A., Rodriguez, J. E., et al. 2023, ApJL, 944, L35
Gillon, M., Triaud, A., Demory, B., et al. 2017, Natur, 542, 456
Greene, T. P., Bell, T. J., Ducrot, E., et al. 2023, Natur, 618, 39
Guerrero, N., & Ballard, S. 2024, ApJ, 975, 256
Hammond, M., & Pierrehumbert, R. 2018, ApJ, 869, 65
Hammond, M., Tsai, S.-M., & Pierrehumbert, R. T. 2020, ApJ, 901, 78
Hammond, T., & Komacek, T. D. 2024, ApJ, 968, 43
Haqq-Misra, J., Wolf, E., Joshi, M., Zhang, X., & Kopparapu, R. 2018, ApJ, 852, 67
Hu, Y., & Yang, J. 2014, PNAS, 111, 629
Johnson, T. M., Kelahan, C., Mandell, A., et al. 2025, A&C, 50, 100890
Joshi, M., Haberle, R., & Reynolds, R. 1997, Icar, 129, 450
Kane, S. R. 2022, NatAs, 6, 420
Kane, S. R., Arney, G., Crisp, D., et al. 2019, JGRE, 124, 2015
Kane, S. R., Arney, G. N., Byrne, P. K., et al. 2021, JGRE, 126, e06643
Kane, S. R., & Byrne, P. K. 2024, NatAs, 8, 417
Kane, S. R., Ceja, A. Y., Way, M. J., & Quintana, E. V. 2018, ApJ, 869, 46
Kane, S. R., Kopparapu, R. K., & Domagal-Goldman, S. D. 2014, ApJL, 794, L5
Kofman, V., Villanueva, G., Fauchez, T., et al. 2024, PSJ, 5, 197
Kofman, V., & Villanueva, G. L. 2021, JQSRT, 270, 107708
Koll, D., & Abbot, D. 2016, ApJ, 825, 99
Koll, D. D. B., Jeevanjee, N., & Lutsko, N. J. 2023, JAtS, 80, 1923
Komacek, T., & Abbot, D. 2019, ApJ, 871, 245
Kopparapu, R., Wolf, E., Arney, G., et al. 2017, ApJ, 845, 5
Kossakowski, D., Kürster, M., Trifonov, T., et al. 2023, A&A, 670, A84
Kreidberg, L., & Loeb, A. 2016, ApJL, 832, L12
Kurucz, R. L. 2005, MSAIS, 8, 14
Labonté, M., & Merlis, T. 2020, ApJ, 896, 31
Lehmer, O. R., Catling, D. C., & Krissansen-Totton, J. 2020, NatCo, 11, 6153
Lewis, N., Lambert, F., Boutle, I., et al. 2018, ApJ, 854, 171
Lim, O., Benneke, B., Doyon, R., et al. 2023, ApJL, 955, L22
Lobo, A. H., & Shields, A. L. 2024, ApJ, 972, 71
Lobo, A. H., Shields, A. L., Palubski, I. Z., & Wolf, E. 2023, ApJ, 945, 161
Lovis, C., & Fischer, D. 2010, in Exoplanets, ed. S. Seager (Tucson, AZ: Univ. Arizona Press),
Lustig-Yaeger, J., Fu, G., May, E. M., et al. 2023, NatAs, 7, 1317
Lustig-Yaeger, J., Meadows, V., & Lincowski, A. 2019, AJ, 158, 27
Lustig-Yaeger, J., Meadows, V. S., & Lincowski, A. P. 2019, ApJL, 887, L11
Lustig-Yaeger, J., Stevenson, K. B., Mayorga, L. C., et al. 2021, ApJL, 921, L4
Macdonald, E., Paradise, A., Menou, K., & Lee, C. 2022, MNRAS, 513, 2761
Mak, M. T., Sergeev, D. E., Mayne, N., et al. 2024, MNRAS, 529, 3971
Manabe, S., & Wetherald, R. T. 1975, JAtS, 32, 3
Mandell, A. M., Lustig-Yaeger, J., Stevenson, K. B., & Staguhn, J. 2022, AJ, 164, 176
May, E., Taylor, J., Komacek, T., Line, M., & Parmentier, V. 2021, ApJL, 911, L30
May, E. M., MacDonald, R. J., Bennett, K. A., et al. 2023, ApJL, 959, L9
Mayorga, L. C., Lustig-Yaeger, J., Stevenson, K. B. & Consortium On HabitabilityAtmospheres Of M-Dwarf Planets (Champs) 2023, ApJ, 956, 74
Merlis, T., & Schneider, T. 2010, JAMES, 2, 13
Mikal-Evans, T. 2022, MNRAS, 510, 980
Millholland, S. C., Lara, T., & Toomlaid, J. 2024, ApJ, 961, 203
Neale, R., Richter, J., Conley, A., et al. 2010, Description of the NCAR Community Atmosphere Model (CAM 4.0) (Boulder, CA: National Center for Atmospheric Research),
Noda, S., Ishiwatari, M., Nakajima, K., et al. 2017, Icar, 282, 1
Ohno, K., & Zhang, X. 2019, ApJ, 874, 1
Ostberg, C., & Kane, S. R. 2019, AJ, 158, 195
Ostberg, C., Kane, S. R., Lincowski, A. P., & Dalba, P. A. 2023a, AJ, 166, 213
Ostberg, C., Kane, S. R., Li, Z., et al. 2023b, AJ, 165, 168
Pierrehumbert, R. 2011, ApJL, 726, L8
Pierrehumbert, R., & Hammond, M. 2019, AnRFM, 51, 275
Quanz, S. P., Ottiger, M., Fontanet, E., et al. 2022, A&A, 664, A21
Rackham, B. V., & de Wit, J. 2024, AJ, 168, 82
Rauscher, E. 2017, ApJ, 846, 69
Rhines, P. 1975, JFM, 69, 417
Rodriguez, J. E., Vanderburg, A., Zieba, S., et al. 2020, AJ, 160, 117
Rotman, Y., Komacek, T. D., Villanueva, G. L., Fauchez, T. J., & May, E. M. 2023, ApJL, 942, L4
Salazar, A., Olson, S., Komacek, T., Stephens, H., & Abbot, D. 2020, ApJL, 896, L16
Seeley, J., Jeevanjee, N., & Romps, D. 2019, GeoRL, 46, 1842
Sergeev, D., Lambert, F., Mayne, N., et al. 2020, ApJ, 894, 84
Sergeev, D., Lewis, N., Lambert, F., et al. 2022, PSJ, 3, 214
Sergeev, D. E., Fauchez, T. J., Turbet, M., et al. 2022, PSJ, 3, 212
Shields, A. 2019, ApJS, 243, 30
Shields, A. L., Ballard, S., & Johnson, J. A. 2016, PhR, 663, 1
Showman, A., Wordsworth, R., Merlis, T., & Kaspi, Y. 2013, in Comparative Climatology of Terrestrial Planets, ed. S. Mackwell et al. (Tucson, AZ: Univ. Arizona Press)
Snellen, I., de Kok, R., Birkby, J., et al. 2015, A&A, 576, A59
Snellen, I. A. G., Désert, J. M., Waters, L. B. F. M., et al. 2017, AJ, 154, 77
Song, X., & Yang, J. 2021, FrASS, 8, 134
Stevenson, K. B. & Space Telescopes Advanced Research Group on the Atmospheres of Transiting Exoplanets 2020, ApJL, 898, L35
Suárez Mascareño, A., González-Álvarez, E., Zapatero Osorio, M. R., et al. 2023, A&A, 670, A5
Suissa, G., Mandell, A. M., Wolf, E. T., et al. 2020a, ApJ, 891, 58
Suissa, G., Wolf, E. T., Kopparapu, R., et al. 2020b, AJ, 160, 118
Turbet, M., Bolmont, E., Chaverot, G., et al. 2021, Natur, 598, 276

Turbet, M., Bolmont, E., Leconte, J., et al. 2018, A&A, 612, A86
Turbet, M., Fauchez, T. J., Leconte, J., et al. 2023, A&A, 679, A126
Turbet, M., Fauchez, T. J., Sergeev, D. E., et al. 2022, PSJ, 3, 211
Turbet, M., Leconte, J., Selsis, F., et al. 2016, A&A, 596, A112
Valencia, D., O'Connell, R. J., & Sasselov, D. 2006, Icar, 181, 545
Vaughan, S. R., Birkby, J. L., Thatte, N., et al. 2024, MNRAS, 528, 3509
Villanueva, G. L., Liuzzi, G., Faggi, S., et al. 2022, Fundamentals of the Planetary Spectrum Generator (Greenbelt, MD: NASA Goddard Space Flight Center),
Villanueva, G. L., Smith, M. D., Protopapa, S., Faggi, S., & Mandell, A. M. 2018, JQSRT, 217, 86
Wang, Y., Read, P., Tabataba-Vakili, F., & Young, R. 2018, QJRMS, 144, 2537
Way, M., Genio, A. D., Aleinov, I., et al. 2018, ApJS, 239, 24
Wei, M., Zhang, Y., & Yang, J. 2020, ApJ, 898, 156
Weiner Mansfield, M., Xue, Q., Zhang, M., et al. 2024, ApJL, 975, L22
Winn, J. 2010, in Exoplanets, ed. S. Seager (Tucson, AZ: Univ. Arizona Press),
Wolf, E. 2017, ApJL, 839, L1
Wolf, E., Haqq-Misra, J., Kopparapu, R., et al. 2020, JGRE, 125, e2020JE006576
Wolf, E., Kopparapu, R., Haqq-Misra, J., & Fauchez, T. 2022, PSJ, 3, 7
Wolf, E. T., Kopparapu, R. K., & Haqq-Misra, J. 2019, ApJ, 877, 35
Xue, Q., Bean, J. L., Zhang, M., et al. 2024, ApJL, 973, L8
Yang, H., Komacek, T., & Abbot, D. 2019, ApJL, 876, L27
Yang, J., Boue, G., Fabrycky, D., & Abbot, D. 2014, ApJL, 787, L2
Yang, J., Cowan, N., & Abbot, D. 2013, ApJL, 771, L45
Yang, J., Zhang, Y., Fu, Z., et al. 2023, NatAs, 7, 1070
Zechmeister, M., Dreizler, S., Ribas, I., et al. 2019, A&A, 627, A49
Zhan, R., Koll, D. D. B., & Ding, F. 2024, ApJ, 971, 125
Zieba, S., Kreidberg, L., Ducrot, E., et al. 2023, Natur, 620, 746